Delay-differential-equation model for mode-locked lasers based on nonlinear optical and amplifying loop mirrors

A. G. Vladimirov [1], S. Suchkov [2], G. Huyet,[3] and S. K. Turitsyn [2,4]

[1]*Weierstrass Institute, Mohrenstrasse 39, 10117 Berlin, Germany*

[2]*Aston-NSU International Centre for Photonics, Novosibirsk State University, 630090 Novosibirsk, Russia*

[3]*Université Côte d'Azur, Centre National de La Recherche Scientifique, Institut de Physique de Nice, 2 Avenue Joseph Vallot, 06108 Nice, France*

[4]*Aston Institute of Photonic Technologies, Aston University, B4 7ET Birmingham, England*

(Received 9 July 2021; accepted 3 September 2021; published 29 September 2021)

Delay differential equation model of a nonlinear optical–nonlinear amplifying loop mirror mode-locked laser is developed that takes into account the finite relaxation rate of the gain medium and asymmetric beam splitting at the entrance of the nonlinear mirror loop. Asymptotic linear stability analysis of the continuous wave solutions performed in the limit of large delay indicates that in a class-B laser flip instability is preceded by the modulational instability and therefore cannot give rise to stable square wave patterns. Numerically it is shown that the model can demonstrate large windows of regular fundamental and harmonic mode-locked regimes with single and multiple pulses per cavity round trip time separated by domains of irregular pulsing.

DOI: 10.1103/PhysRevA.104.033525

I. INTRODUCTION

Passively mode-locked lasers have attracted much attention in recent decades due to their numerous applications in science, biomedicine, and industry. In passive mode-locking the presence of saturable absorption in the laser cavity is needed to allow short pulse generation. Among different mechanisms to create saturable absorption, a promising one relies on the use of the nonlinear optical–nonlinear amplifying loop mirror (NOLM-NALM) [1], which contains a bidirectional loop with asymmetrically located absorber or gain medium and nonlinear element. These configurations are also known as figure-eight lasers [2,3]. As a result of the interference of two counterpropagating waves, the reflectivity of the NOLM-NALM depends strongly on the power of the incident beam, which creates an effective saturable absorption mechanism.

Most of the models used for theoretical analysis of NOLM-NALM mode-locked lasers are based on the NLS- and Ginzburg-Landau-type equations (see, e.g., [4–10] and references therein), where the dynamics of the gain is determined by the average intracavity laser power. An alternative approach to the modeling of NOLM-NALM lasers was proposed in [11], where a simple delay differential equation (DDE) model of a nonlinear mirror mode-locked laser was developed using the approach of the authors of [12–14] and analyzed analytically and numerically. Later a similar DDE model was used in [15] to describe a mode-locking in a NALM mode-locked laser with a semiconductor optical amplifier (SOA) in the nonlinear mirror loop. Both these models, however, assumed adiabatic elimination of the inversion in the gain medium and symmetric beam splitter connecting the main laser cavity with the nonlinear mirror loop. On the other hand, asymmetric beam splitters are widely used in nonlinear mirror mode-locked lasers, see, e.g., [4,16–19]. Furthermore, as soon as the pulse duration becomes smaller than the gain relaxation time the effect of the gain dynamics on the pulse shaping must be taken into account [20]. An empirical NOLM model including a rate equation for the population inversion dynamics was reported in [17]. However, since such an important physical factor as spectral filtering of the laser radiation is missing in this model, similarly to the Poincaré map model used in [21], it is hardly applicable to describe short pulse generation in mode-locking regimes. The aim of this paper is to generalize the model developed in [11] to the case of arbitrary population relaxation rates of the laser gain medium and beam splitting ratios. Note that, similarly to the models discussed in [11,15], our model assumes that mode-locked pulses are sufficiently long so that chromatic dispersion of the intracavity medium does not play an important role in the mechanism of the mode-locked pulse formation. Although the chromatic dispersion can be included into DDE laser models [22–25] and Ikeda-map models [26], this task is beyond the scope of the present work. The lumped element approach used to derive the NOLN-NALM laser model assumes that gain, linear loss, Kerr nonlinearity, and Lorentzian spectral filtering are separated in space in the laser cavity and attributed to different laser sections. Furthermore, we assume that the spectral filtering section is thin.

Using the generalized model, we investigate analytically the stability and bifurcations of continuous wave (CW) solutions in the limit of large delay. Numerical simulations reveal large domains of fundamental and harmonic mode-locking regimes in the parameter space. We show that both the inversion relaxation rate and beam splitting ratio can strongly affect the dynamics of the system and the existence domains of stable mode-locked regimes.

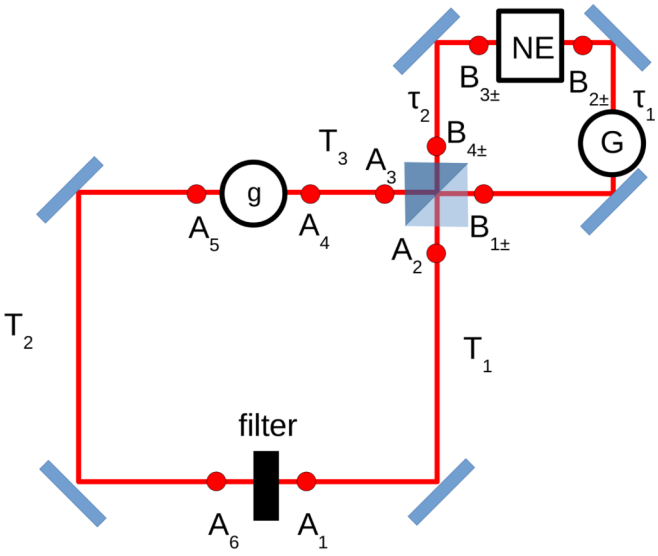

FIG. 1. Schematic representation of the NOLN-NALM laser. g is the amplifying medium in the main cavity, G the linear loss or gain in the nonlinear mirror loop, NE is the nonlinear element, $A_{1,2,3,4,5,6}$ the electric field envelopes in the main cavity (unidirectional, counterclockwise), and $B_{\pm1,\pm2,\pm3,\pm4}$ the electric field envelopes in the nonlinear mirror loop (bidirectional). Here the subscripts "+" and "−" correspond to counterclockwise and clockwise waves, respectively.

II. MODEL EQUATIONS

In this section we extend the NOLM-NALM mode-locked laser model proposed in [11] to the case of finite gain relaxation rate and arbitrary beam splitting ratio. A schematic presentation of the laser system under consideration is given in Fig. 1. A commonly used figure-of-eight NOLM-NALM laser contains a bidirectional nonlinear mirror loop coupled to the main cavity, where an optical isolator is used to achieve unidirectional operation [3,4,8,9,15–17,19,27].

To derive our model equations we use the lumped element approach similar to that described in [12–14]. Propagation of the electric field envelope in the passive sections of the main unidirectional cavity can be described by the relations

$$A_2(t) = \sqrt{\kappa_2}A_1(t - T_1), \quad A_4(t) = A_3(t - T_3),$$
$$A_6(t) = \sqrt{\kappa_1}A_5(t - T_2), \tag{1}$$

where $0 < \kappa_{1,2} < 1$ are the intensity attenuation factors due to the linear nonresonant losses in the intracavity media and output of radiation through the mirrors. $T_{1,2}$ are the delay times introduced by the passive sections.

The gain section of the main cavity can be described by the relation

$$A_5(t) = A_4(t - T_4)e^{\frac{1-i\alpha}{2}g(t)}, \tag{2}$$

where α is the linewidth enhancement factor, which is nonzero in the case when SOA is used as a gain medium. The experimental study of a NOLM mode-locked laser with SOA amplifying medium was reported in [28]. The time evolution of the cumulative gain $g(t)$ is governed by the ordinary differential equation [14,29]

$$\gamma^{-1}\frac{dg}{dt} = p - g - (e^g - 1)|A_4(t - T_4)|^2. \tag{3}$$

Here γ is the normalized gain relaxation rate and p is the linear gain (pump) parameter.

The transformations of the counterpropagating field amplitudes by the linear gain (loss) and passive sections of the nonlinear mirror loop are given by

$$B_{-1}(t) = \sqrt{G}B_{-2}(t - \tau_1), \quad B_{+2} = \sqrt{G}B_{+1}(t - \tau_1),$$
$$B_{-1}(t) = B_{-2}(t - \tau_2), \quad B_{+4}(t) = B_{+3}(t - \tau_2), \tag{4}$$

where $G > 1$ ($G < 1$) correspond to NALM (NOLM), the subscript "+" ("−") denotes counterclockwise (clockwise) propagating wave, and $\tau_{1,2}$ are the corresponding delay times, which depend on the length of the passive sections of the nonlinear mirror loop. For the Kerr element inside this loop we can write

$$B_{-2}(t) = B_{-3}(t - \tau_3)e^{-ia[|B_{-3}(t-\tau_3)|^2 + h|B_{+2}(t-\tau_3)|^2]},$$
$$B_{+3}(t) = B_{+2}(t - \tau_3)e^{-ia[|B_{+2}(t-\tau_3)|^2 + h|B_{-3}(t-\tau_3)|^2]}, \tag{5}$$

where a and τ_3 are the Kerr coefficient and time delay introduced by the nonlinear element, respectively. Both these quantities are proportional to the length of the nonlinear element. The parameter h is responsible for the standing wave effect. Since in the mode-locking regime when the pulse duration is much smaller then the cavity round trip time one can neglect the interference of the two counterpropagating pulses in the nonlinear element; below we assume that $h = 0$ in Eq. (5).

The beam splitter with $K : 1 - K$ intensity ratio is described by

$$B_{+1}(t) = -\sqrt{K}A_2(t), \quad B_{-4}(t) = \sqrt{1 - K}A_2(t),$$
$$A_3(t) = \sqrt{1 - K}B_{-1}(t) + \sqrt{K}B_{+2}(t), \tag{6}$$

where $0 < K < 1$ and the sign "−" in the first equation corresponds to the reflection from a more dense medium. $K = 0.5$ corresponds to a symmetric 50 : 50 splitter.

Finally, the thin Lorentzian spectral filtering element is described by

$$\Gamma^{-1}\frac{dA_1(t)}{dt} + A_1(t) = A_6(t). \tag{7}$$

Below we assume that the time t is normalized in such a way that the spectral width of the filter is $\Gamma = 1$. In this case the inversion relaxation rate in Eq. (3) is normalized by the spectral filter width $\gamma = (\tau_g\Gamma)^{-1}$, where τ_g is the dimensional inversion relaxation time. Note that the inverse filter spectral width Γ^{-1} gives approximately the lower limit for the pulse width τ_p generated by the NOLM-NALM mode-locked laser. Therefore, we get the relation $\gamma \lesssim \tau_p/\tau_g$.

Substituting the relations (1) to (7) into one another we obtain our master NOLM-NALM laser model

$$\frac{dA}{dt} + A = \sqrt{\kappa}e^{(1-i\alpha)g/2 + i\theta}r(|A_T|^2)A_T, \tag{8}$$

$$\gamma^{-1}\frac{dg}{dt} = p - g - (e^g - 1)|A_T|^2|r(|A_T|^2)|^2, \tag{9}$$

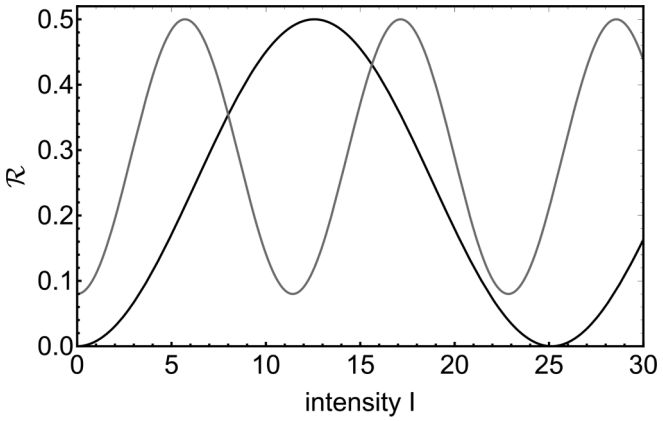

FIG. 2. Intensity reflectivity $\mathcal{R}$ of the nonlinear mirror defined by Eq. (11) as a function of the field intensity $I = |A|^2$. Black (gray) line corresponds to symmetric (asymmetric) beam splitter, $K = 0.5$ ($K = 0.3$). Other parameters are $a = 1.0$ and $G = 0.5$.

where $A \equiv A_1, \kappa = \kappa_1\kappa_2$ describes the total linear nonresonant losses in the main cavity per round trip $0 < \kappa < 1$, the subscript T denotes the delayed argument, $A_T = A(t - T)$ with the delay time $T = T_1 + T_2 + T_3 + T_4 + \tau_1 + \tau_2 + \tau_3$ equal to the normalized cold cavity round trip time, and the complex nonlinear mirror amplitude reflection coefficient r is given by

$$r(|A_T|^2) = \sqrt{G}[(1 - K)e^{iX_T} - Ke^{iY_T}],$$

with

$$X_T = -a(1 - K)|A_T|^2, \quad Y_T = -aKG|A_T|^2. \tag{10}$$

The intensity reflectivity coefficient $\mathcal{R}$ ($0 \leqslant \mathcal{R} \leqslant G$) of the nonlinear mirror is given by

$$\begin{aligned}\mathcal{R}(|A|^2) &= |r(|A|^2)|^2 \\ &= G(1 - 2K(1 - K)\{1 + \cos(a(1 - K - GK)|A|^2)\}) \\ &= G\left(1 - 4K(1 - K)\cos\left[\frac{a}{2}(1 - K - GK)|A|^2\right]^2\right).\end{aligned} \tag{11}$$

This coefficient coincides with that reported in [1,21,30]. The dependence of the coefficient $\mathcal{R}$ on the laser field intensity $I = |A|^2$ is illustrated in Fig. 2 for the case of 50 : 50 and 30 : 70 beam splitter. It is seen that for symmetric beam splitting the reflectivity is zero at $I = 0$. This is the result of the destructive interference of the two waves counterpropagating in the nonlinear mirror loop, which have equal amplitudes and phase difference π introduced by the splitter in the limit when input intensity tends to zero. With the increase of the input field intensity the amplitudes of the counterpropagating waves remain equal, but acquire additional nonlinear phase difference, which grows linearly with the input intensity. This phase difference appears due to the asymmetry of the loop, where one wave is attenuated first and then experiences the intensity-dependent phase shift in the Kerr element, while the other wave first acquires the phase shift and is attenuated only afterwards. As a result, the reflectively oscillates with the intensity between 0 (destructive interference) and G (constructive interference) with the period $4\pi/[a(1 - K - GK)]$.

If, on the other hand, the beam splitter is asymmetric, the amplitudes of the two waves are always different and their destructive interference never results in zero output. The minimal reflectivity of the nonlinear mirror is then given by $\mathcal{R}_{\min} = G(1 - 2K)^2 > 0$.

III. CW REGIMES

The trivial solution of Eqs. (8) and (9) corresponding to the laser off regime is given by $A = 0$ and $g = p$. This solution is stable below the linear threshold defined by $\kappa\mathcal{R}(0)e^p = 1$, where $\mathcal{R}(0) = G(1 - 2K)^2$. It is seen from this expression that the threshold value of the pump parameter $p = p_0$ is minimal for $K = 0$ and $K = 1$, $p_0 = -\ln(\kappa G)$, and tends to infinity for $K \to 0.5$. This means that for the symmetric beam splitter the laser off solution is always stable [11]. Note that since the linear gain in the nonlinear mirror loop cannot exceed the total losses in the cavity the product κG should be less than unity. All our calculations below are performed for the case of NOLM when $G < 1$ and the condition $\kappa G < 1$ is satisfied automatically.

Nontrivial continuous wave (CW) solutions of Eqs. (8) and (9), $A(t) = A_0e^{i\omega t}$ and $g = g_0$, are defined by

$$\frac{\kappa\mathcal{R}(I_0)e^{g_0}}{1 + \omega^2} = 1, \tag{12}$$

$$p - g_0 - (e^{g_0} - 1)I_0\mathcal{R}(I_0) = 0, \tag{13}$$

$$\begin{aligned}&\tan\left(\omega T + \frac{1}{2}\alpha g_0\right) \\ &= \frac{K(\sin Y_0 - \omega\cos Y_0) - (1 - K)(\sin X_0 - \omega\cos X_0)}{K(\omega\sin Y_0 - \cos Y_0) - (1 - K)(\omega\sin X_0 - \cos X_0)},\end{aligned} \tag{14}$$

where $X_0 = X(I_0)$, $Y_0 = Y(I_0)$, and $I_0 = |A_0|^2$. These solutions can be interpreted as longitudinal laser modes. Equation (12) can be considered as an energy balance condition, which states that the total losses in the cavity are compensated by the amplification. The intensities I_0 of different solutions of Eqs. (12) and (13) are shown in Fig. 3 by gray lines as functions of the pump parameter p. The black line shows the envelope of these solutions obtained by substituting $\omega = 0$ into Eq. (12). It is seen that CW solutions of the the model equations can exhibit a multistable behavior.

The solutions of Eqs. (12) and (13) are shown in Fig. 4 for several different values of the pump parameter p by thick colored curves on the (I_0, ω) plane, while the solutions of Eq. (14) are indicated by thin gray lines. The intersections of the thick-colored lines with the thin gray lines correspond to CW longitudinal laser modes. The density of gray lines increases with T, so that in the limit $T \to \infty$ the modes densely fill the colored curves. Therefore, in this limit the thick-colored curves in Fig. 4 defined by Eqs. (12) and (13) determine the locus of the CW laser modes. A representation of this locus as a two-dimensional (2D) surface in the three-dimensional (3D) space (p, ω, I_0) is shown in Fig. 5.

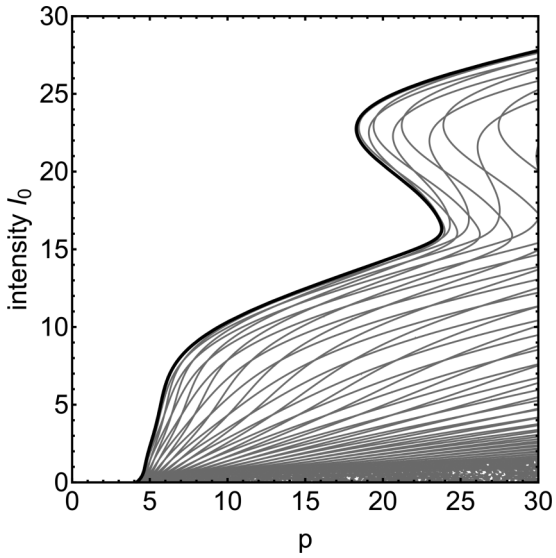

FIG. 3. CW solutions of the model equations (8) and (9) as functions of the pump parameter p (gray lines). Black line is obtained by substituting $\omega = 0$ into Eq. (12). Parameters are $\kappa = 0.8$, $a = 1.0$, $\alpha = 0$, $T = 25$, $K = 0.4$, and $G = 0.5$.

IV. LINEAR STABILITY ANALYSIS IN THE LIMIT OF LARGE DELAY

In the large delay limit $T \to \infty$ we assume that the CW solutions of Eqs. (8) and (9) densely fill the locus of the CW solutions defined by Eqs. (12) and (13). In this case we can forget about Eq. (14) and consider the frequency ω of the CW solutions as a pseudocontinuous variable. The bifurcation diagram calculated in the limit $T \to \infty$ is shown in Fig. 6. In this figure linear laser threshold defined by the condition

$$\frac{\kappa \mathcal{R}(0) e^{p}}{1+\omega^2} = 1$$

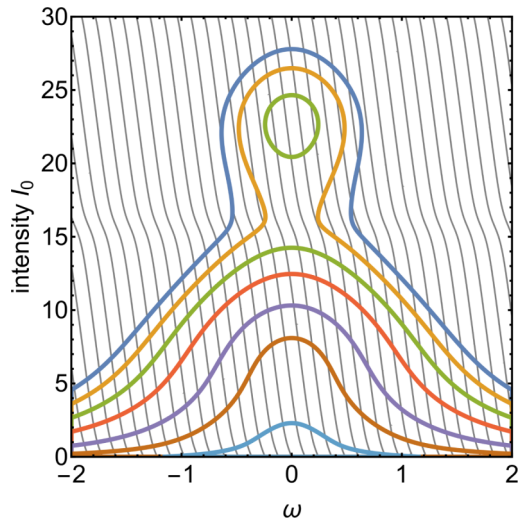

FIG. 4. CW solutions (longitudinal laser modes) on the (I_0, ω) plane correspond to the intersections of thick-colored curves with thin gray lines. Different colors correspond to the pump parameter values $p = 4.0$, $p = 4.5$, $p = 6.5$, $p = 10.0$, $p = 13.0$, $p = 17.0$, and $p = 25.0$. Other parameters are the same as in Fig. 3.

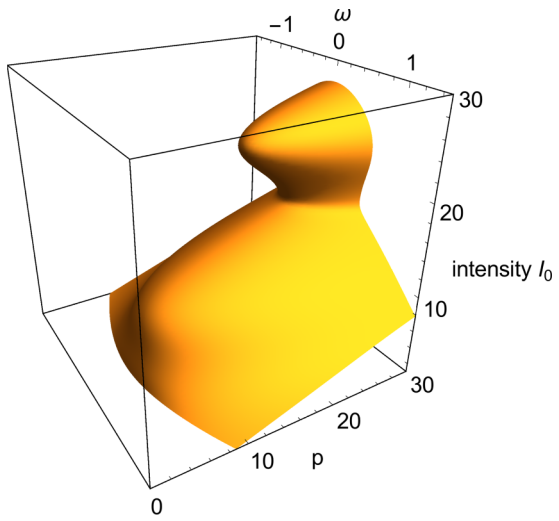

FIG. 5. Locus of the CW longitudinal laser modes in the limit $T \to \infty$. Parameters are the same as in Fig. 3.

is indicated by black line on the (ω, p) plane.

The linear stability of a nontrivial CW solution with the frequency ω is determined by the solutions λ of the characteristic equation

$$c_2(\lambda) Y^2 + c_1(\lambda) Y + c_0(\lambda) = 0, \tag{15}$$

where

$$Y = e^{-\lambda T},$$

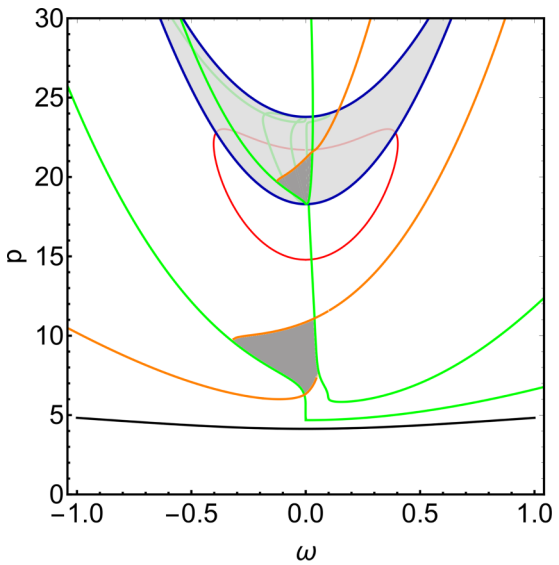

FIG. 6. Two-parameter bifurcation diagram of the CW solutions in the limit $T \to \infty$. Light gray area shows bistability domain where the solutions of Eqs. (12) and (13) have three nontrivial solutions for $I_0 > 0$. This area is limited by the saddle-node instability boundary indicated by the blue line. Dark gray areas indicate the stability domains of CW regimes. Green line indicates long wavelength modulation instability, orange line shows the short wavelength modulation instability, and the red line represents the flip instability. $\gamma = 0.05$. Other parameters are the same as in Fig. 3.

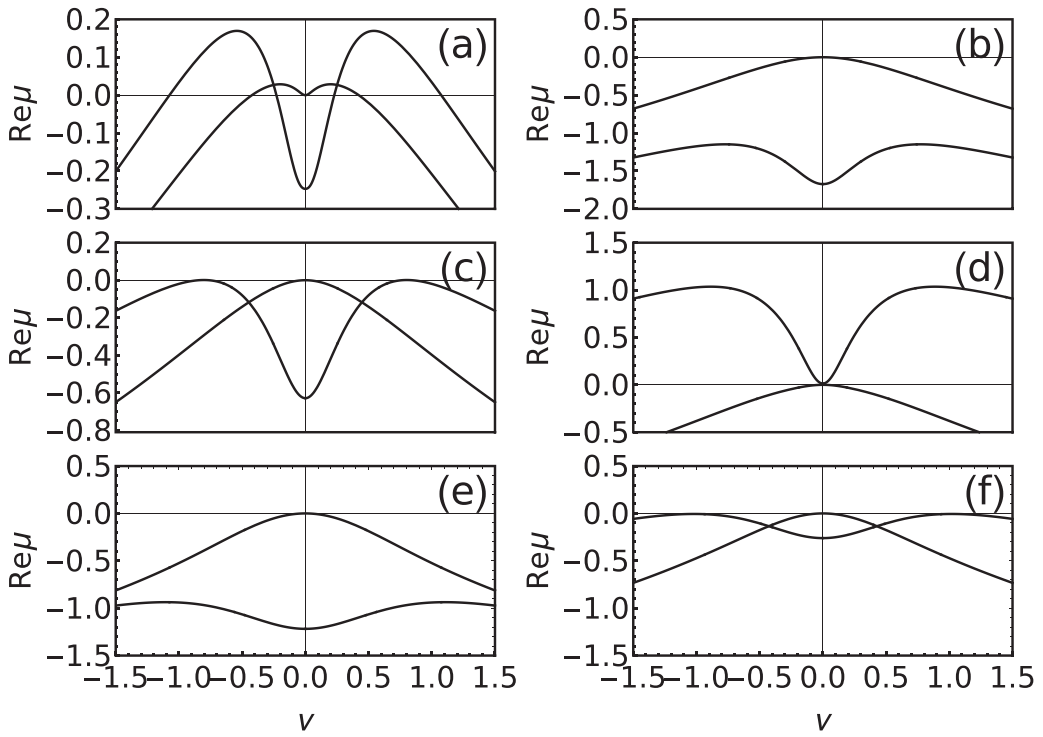

FIG. 7. Real parts of the eigenvalues $\mu(\nu)$. Two curves correspond to μ_1 and μ_2, where μ_2 is responsible for the long wavelength instability and always has zero real part at $\nu = 0$. $\omega_0 = -0.02$. (a) $p = 6.0$. (b) $p = 9.0$. (c) $p = 10.75$. (d) $p = 15.0$. (e) $p = 19.7$. (f) $p = 20.9$. Other parameters are the same as in Fig. 6.

and the expressions for the coefficients $c_0(\lambda)$, $c_1(\lambda)$, and $c_2(\lambda)$ are given in the Appendix.

In the limit $T \to \infty$ the pseudocontinuous spectrum $\mu(\nu)$ of the CW solutions is obtained by solving the characteristic Eq. (15) with respect to Y, $Y = Y_{1,2}(\lambda)$, and performing the substitution $\lambda \to i\nu$ in the resulting solution [31]

$$\mu(\nu) = -\ln[Y(i\nu)].$$

The saddle-node and flip instabilities of CW solutions are defined by the condition that the first solution of the characteristic Eq. (15) satisfies the conditions

$$Y_1(0) = 1 \tag{16}$$

and

$$Y_1(0) = -1, \tag{17}$$

respectively, with

$$Y_1(0) = \frac{\kappa + I_0(1+\omega^2)}{\kappa[1 + I_0\mathcal{R}(I_0)]\left[1 + I_0\frac{d\ln\mathcal{R}(I_0)}{dI_0}\right]}. \tag{18}$$

It follows from Eq. (18) that the saddle-node and flip instability conditions do not depend on the gain relaxation rate γ. The saddle-node instability condition (16) defines the folds of CW locus surface shown in Fig. 5. The flip instability (17) is responsible for a period-doubling cascade giving rise to more and more complicated square wave patterns with increasing periods [11]. The light gray area in Fig. 6 indicates the bistability domain, where for every given frequency ω there are three nontrivial solutions of Eqs. (12) and (13) with $I_0 > 0$. This domain is limited by the saddle-node instability boundary shown by the blue line. The red line indicates the flip instability.

Unlike the flip and saddle-node instabilities, the short- and long-wavelength modulational instabilities of the CW solutions depend on the normalized inversion relaxation rate γ. The second solution $Y_2(\lambda)$ of the characteristic Eq. (15) has the property $Y_2(0) = 1$ or equivalently $\mu_2(0) = 0$, which corresponds to the phase-shift symmetry of the model Eqs. (8) and (9), $A(t) \to A(t)e^{i\phi}$ with arbitrary ϕ. The long-wavelength modulational instability is defined by the condition

$$\mathrm{Re}[\partial_{\nu\nu}\mu_2(\nu)]_{\nu=0} = \mathrm{Re}\{\partial_{\nu\nu}[-\ln Y_2(i\nu)]\}_{\nu=0} = 0.$$

It is shown by the green lines in Fig. 6. Another type of the modulational instability of CW solutions of Eqs. (8) and (9) is the short-wavelength instability which corresponds to the situation when the pseudocontinuous spectral curve touches the imaginary axis at the points $\nu = \pm\nu_0$ with $\nu_0 > 0$, i.e.,

$$\mathrm{Re}[\mu_1(\nu_0)] = \mathrm{Re}[\partial_\nu\mu_1(\nu)]_{\nu=\nu_0} = 0,$$

where $\mu_1 = -\ln Y_1(i\nu)$. This instability is shown in Fig. 6 by the orange lines. It is seen that all the CW solutions are unstable to short- and long-wave modulations already at the threshold [see Fig. 7(a)] for any frequency ω and are stabilized in the lower dark gray area after crossing the respective lines with increasing p [see Fig. 7(b)]. Unlike the case of adiabatically eliminated gain, where (in a certain range of frequency detunings) flip instability occurs on stable CW solutions before the modulational instability and gives rise to a formation of stable square wave patterns [11], for the parameters of Fig. 6 corresponding to a relatively slow inversion relaxation,

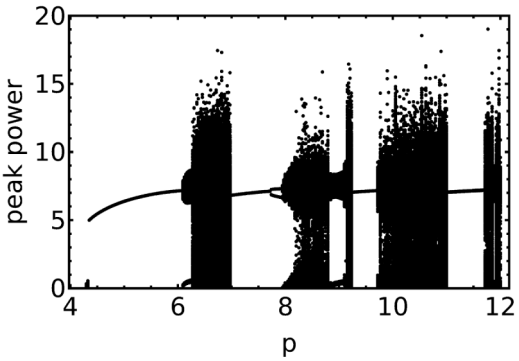

FIG. 8. Bifurcation tree illustrating the pulse peak power as function of the pump parameter p. $\kappa = 0.8$, $a = 1.0$, $\alpha = 0$, $T = 25$, $K = 0.4$, $G = 0.5$, and $\gamma = 0.05$.

flip bifurcation always occurs on CW solutions which are already modulationally unstable. Therefore, branching of the stable square wave patterns from CW solutions via a cascade of flip bifurcations is not possible for such parameter values. Real parts of the eigenvalues μ corresponding to the pump parameter values close to short-wavelength modulational and flip instabilities are shown in Figs. 7(c) and 7(d), respectively. It is seen that both these instabilities are associated with the same eigenvalue branch μ_1. Finally, the two bottom panels in Fig. 7 illustrate the pseudocontinuous eigenvalue spectrum within the upper dark gray area [Fig. 7(e)] and short-wavelength modulational instability at the upper boundary of this area [Fig. 7(f)]. Note that to avoid overloading of Fig. 6 we do not show in this figure the bifurcations of the unstable branch of CW solutions having negative slope on the (p, I_0) plane, see, e.g., the black line in Fig. 3.

V. NUMERICAL RESULTS

The bifurcation tree obtained by numerical integration of Eqs. (8) and (9) is shown in Fig. 8. The black dots in this figure correspond to the local maximums of the laser field intensity time trace (pulse peak powers) calculated after the transient time of 4000 cavity round trips. For a given pump parameter value where the laser exhibits a regular mode-locked regime all the dots coincide and have their ordinate equal to the pulse peak power. Irregular pulsing behavior corresponds to a cloud of dots having different ordinates corresponding to different pulse peak powers. The bifurcation tree in Fig. 8 shows four windows of regular mode-locking regimes separated by the domains of irregular pulsing. The first, second, third, and fourth windows correspond to a regime with one, two, three, and four pulses per cavity round trip, respectively. The fundamental mode-locking regime is illustrated in Fig. 9(a), while the harmonic mode-locked regimes with two, three, and four pulses per cavity round trip time are shown in Figs. 9(b)–9(d), respectively. It is seen that, although initially the pulse peak power of the fundamental mode-locking regime grows with the pump parameter p, the further increase of p leads to an increase of the number of pulses per cavity round trip time, while the pulse peak power and shape remain almost unchanged. The pulses shown in Fig. 9 are asymmetric with slowly decaying trailing edge due to relatively slow relaxation

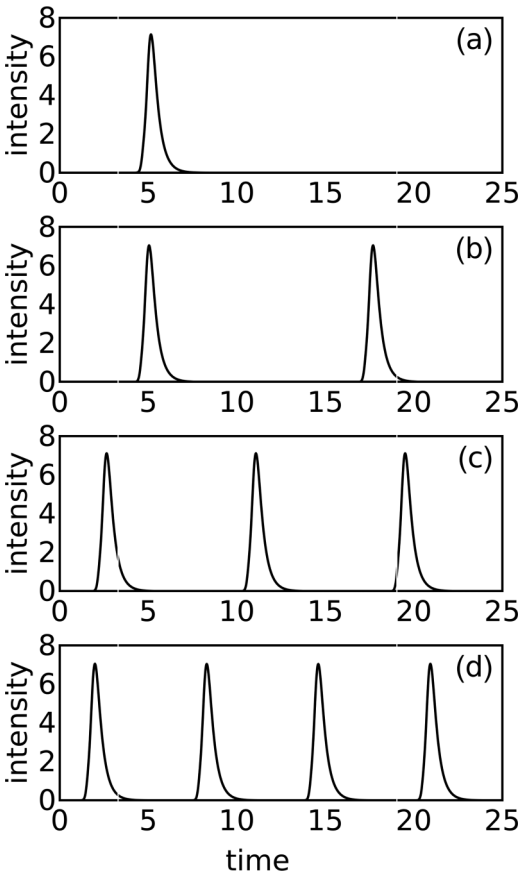

FIG. 9. Fundamental mode-locking regime (a) $p = 6.0$. Harmonic mode-locking regimes with two (b) $p = 7.5$, three (c) $p = 9.5$, and four (d) $p = 11.5$, pulses per cavity round trip time. Other parameters are the same as in Fig. 8.

of the gain. Note that, unlike the case of the 50 : 50 beam splitter [11], where mode-locked pulses are always bistable with the laser off state, for the parameter values of Fig. 8 corresponding to an asymmetric 40 : 60 splitter stable mode-locked pulses exist above the linear laser threshold, where the laser off solution is unstable. Figure 10 is similar to Fig. 8 and shows the evolution of the mean power with the pump parameter p. This figure gives an idea how the number of pulses per cavity round trip increases with the pump power.

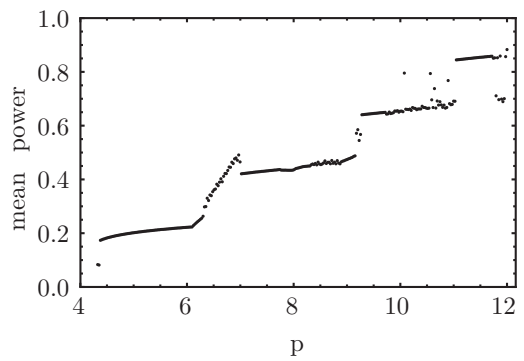

FIG. 10. Same as Fig. 8 but with mean laser power instead of peak power on the y axis. Parameters are the same as in Fig. 8.

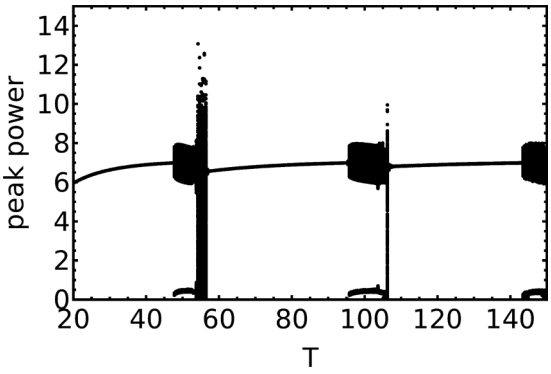

FIG. 11. Bifurcation tree similar to that shown in Fig. 8, but obtained by changing the cold cavity round trip time T. $p = 5$. Other parameters are the same as in Fig. 8.

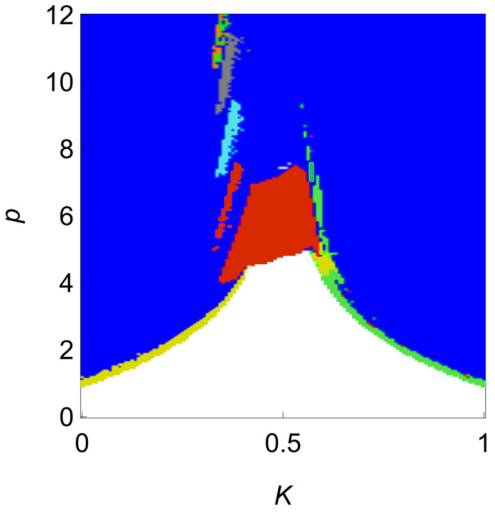

FIG. 12. Map of different dynamical regimes in the (K, p) plane. White color indicates laser off regime, yellow is the CW solutions, and green are the weakly periodically modulated CW solutions. Red areas correspond to fundamental mode-locked regime with a single pulse per cavity round trip. Cyan, gray, and orange show harmonic mode-locked regimes with two, three, and four pulses per cavity round trip. Blue color indicates irregular pulsing. Parameters are the same as in Fig. 8.

In Fig. 11, a bifurcation tree similar to that shown in Fig. 8 is presented, but obtained by increasing the delay parameter T, three windows of regular mode-locking solutions are separated by thin domains of irregular pulsing. Here the first, second, and third mode-locking windows correspond to regular mode-locking regimes with one, two, and three pulses per cavity round trip time. These regimes are similar to those shown in Figs. 9(a)–9(c).

Our numerical simulation shows that for certain parameter values the solutions of the model equations can exhibit bistability or multistability when choosing different initial conditions. In particular, it follows from Figs. 6 and 8 that stable mode-locked pulses can coexist with stable CW regimes. In addition, these pulses can coexist with irregular pulsed regimes and, when K is sufficiently close to 0.5, with the laser off state. A numerically calculated map of the dynamical regimes is shown in Fig. 12 in the two-parameter plane (K, p). It was obtained by integration of Eqs. (8) and (9) with the initial condition in the form of the Gaussian pulse $A(t) = A_m \exp[-(t + 0.5T)^2/w^2]$ and $g(t) = p$ on the interval $t \in [-T, 0]$, where $A_m = 2$ and $w = 4$. The red color in Fig. 12 indicates the regions of the fundamental mode-locked regime with a single pulse per cavity round trip. The regions of the harmonic mode-locked regimes with two, three, and four pulses per cavity round trip are shown by the cyan, gray, and orange colors, respectively. The white color corresponds to the laser off regime. The yellow and green colors indicate stable and weakly periodically modulated CW regimes, respectively. It is seen from Fig. 12 that the domain of the fundamental mode-locked regime is asymmetric in K and located around $K = 0.5$ and that the use of slightly asymmetric beam splitter could help to achieve stable harmonic mode-locked regimes.

VI. CONCLUSION

We developed and analyzed a DDE NOLM-NALM mode-locked laser model taking into account an arbitrary inversion relaxation rate in the gain medium as well as the asymmetry of the beam splitter. Our numerical simulations indicate that with increasing pump parameter this model can exhibit large windows of regular fundamental and harmonic mode-locked regimes separated by regions of irregular pulsing. The experimental observation harmonic mode-locking regimes in NOLM-NALM lasers was reported in [10,27,32]. We showed that, unlike the laser with a symmetric beam splitter where the mode-locked pulses always coexist with a stable laser off solution, a laser with an asymmetric beam splitter can exhibit regular mode-locked regimes above the linear lasing threshold where the laser off solution is unstable. Our numerical simulations reveal that a proper choice of the beam splitting ratio can favor the development of harmonic mode-locked regimes. Furthermore, we demonstrated that for sufficiently slow relaxation of the gain inversion flip bifurcation always takes place on modulationally unstable CW solutions and hence, unlike the case of fast gain recovery, cannot lead to a generation of stable square wave patterns. This bifurcation was predicted theoretically using a Poincaré map NOLM-NALM laser model [21] as well as DDE models with adiabatically eliminated gain [11,15]. The experimental observation of square wave patterns was reported in [15], in a NALM laser with SOA amplifier in the nonlinear mirror loop. On the other hand, the experimental studies of the authors of [21] have not revealed the period doubling cascade predicted theoretically in the same paper. We believe that this work could create a theoretical basis for further steps in modeling of specific types of lasers, for instance, including into consideration the effect of chromatic dispersion of the intracavity media.

ACKNOWLEDGMENTS

We gratefully acknowledge the support by the Deutsche Forschungsgemeinschaft (DFG-RSF Project No. 445430311). The work of S.S. and S.K.T. was supported by the Russian Science Foundation (RSF-DFG Project No. 21-42-04401).

APPENDIX: COEFFICIENTS OF THE CHARACTERISTIC EQUATION (15)

The coefficients $c_{0,1,2}(\lambda)$ in the characteristic Eq. (15) are given by

$$c_0(\lambda) = [(1+\lambda)^2+\omega^2]\left[\gamma + \frac{\gamma I_0}{\kappa}(1+\omega^2) + \lambda\right],$$

$$c_1 = -(1+\lambda+\omega^2)\left\{2(\gamma+\lambda) + \frac{\gamma I_0}{\kappa}[1+\omega^2+\kappa\mathcal{R}(I_0)] + I_0[\gamma+\lambda+\gamma I_0\mathcal{R}(I_0)]\frac{d\ln\mathcal{R}(I_0)}{dI_0}\right\}$$
$$- \lambda\omega W\left[\gamma+\lambda+\frac{\gamma I_0}{\kappa}(1+\omega^2)\right],$$

$$c_2(\lambda) = (1+\omega^2)[\gamma+\gamma I_0\mathcal{R}(I_0)+\lambda]\left[1+I_0\frac{d\ln\mathcal{R}(I_0)}{dI_0}\right],$$

where $W = aI_0[\frac{(1-2K)(1-K-GK)}{\mathcal{R}(I_0)} + 1 - (1-G)K]$ and $I_0 = |A_0|^2$ is the CW intensity obtained from the solution of Eqs. (12) and (13).

[1] N. Doran and D. Wood, Opt. Lett. **13**, 56 (1988).
[2] D. Richardson, R. Laming, D. Payne, V. Matsas, and M. Phillips, Electron. Lett. **27**, 542 (1991).
[3] I. Duling, Electron. Lett. **27**, 544 (1991).
[4] J. Theimer and J. Haus, J. Mod. Opt. **44**, 919 (1997).
[5] M. Salhi, A. Haboucha, H. Leblond, and F. Sanchez, Phys. Rev. A **77**, 033828 (2008).
[6] D. Li, L. Li, J. Zhou, L. Zhao, D. Tang, and D. Shen, Sci. Rep. **6**, 1 (2016).
[7] S. Smirnov, S. Kobtsev, A. Ivanenko, A. Kokhanovskiy, A. Kemmer, and M. Gervaziev, Opt. Lett. **42**, 1732 (2017).
[8] J.-H. Cai, H. Chen, S.-P. Chen, and J. Hou, Opt. Express **25**, 4414 (2017).
[9] S. Boscolo, C. Finot, I. Gukov, and S. K. Turitsyn, Laser Phys. Lett. **16**, 065105 (2019).
[10] D. Deng, H. Zhang, Q. Gong, L. He, D. Li, and M. Gong, Opt. Laser Technol. **125**, 106010 (2020).
[11] A. G. Vladimirov, A. V. Kovalev, E. A. Viktorov, N. Rebrova, and G. Huyet, Phys. Rev. E **100**, 012216 (2019).
[12] A. G. Vladimirov, D. Turaev, and G. Kozyreff, Opt. Lett. **29**, 1221 (2004).
[13] A. G. Vladimirov and D. Turaev, Radiophys. Quantum Electron. **47**, 857 (2004).
[14] A. G. Vladimirov and D. Turaev, Phys. Rev. A **72**, 033808 (2005).
[15] A. Aadhi, A. V. Kovalev, M. Kues, P. Roztocki, C. Reimer, Y. Zhang, T. Wang, B. E. Little, S. T. Chu, Z. Wang *et al.*, Opt. Express **27**, 25251 (2019).
[16] T. V. A. Tran, K. Lee, S. B. Lee, and Y.-G. Han, Opt. Express **16**, 1460 (2008).
[17] L. Yang, L. Zhang, R. Yang, L. Yang, B. Yue, and P. Yang, Opt. Commun. **285**, 143 (2012).
[18] L. Yun, X. Liu, and D. Mao, Opt. Express **20**, 20992 (2012).
[19] J. Li, Z. Zhang, Z. Sun, H. Luo, Y. Liu, Z. Yan, C. Mou, L. Zhang, and S. K. Turitsyn, Opt. Express **22**, 7875 (2014).
[20] M. Nizette and A. G. Vladimirov, Phys. Rev. E **104**, 014215 (2021).
[21] W. J. Lai, P. Shum, and L. Binh, IEEE J. Quantum Electron. **41**, 986 (2005).
[22] A. Pimenov, S. Slepneva, G. Huyet, and A. G. Vladimirov, Phys. Rev. Lett. **118**, 193901 (2017).
[23] A. Pimenov, S. Amiranashvili, and A. G. Vladimirov, Math. Model. Nat. Phenom. **15**, 47 (2020).
[24] C. Schelte, P. Camelin, M. Marconi, A. Garnache, G. Huyet, G. Beaudoin, I. Sagnes, M. Giudici, J. Javaloyes, and S. V. Gurevich, Phys. Rev. Lett. **123**, 043902 (2019).
[25] C. Schelte, D. Hessel, J. Javaloyes, and S. V. Gurevich, Phys. Rev. Appl. **13**, 054050 (2020).
[26] D. A. Zezyulin, V. V. Konotop, and M. Taki, Opt. Lett. **36**, 4623 (2011).
[27] Z. X. Zhang, Z. Q. Ye, M. H. Sang, and Y. Y. Nie, Laser Phys. Lett. **5**, 364 (2008).
[28] T. Cai and L. R. Chen, Opt. Express **18**, 18113 (2010).
[29] G. P. Agrawal and N. A. Olsson, IEEE J. Quantum Electron. **25**, 2297 (1989).
[30] M. E. Fermann, F. Haberl, M. Hofer, and H. Hochreiter, Opt. Lett. **15**, 752 (1990).
[31] S. Yanchuk and M. Wolfrum, SIAM J. Appl. Dyn. Syst. **9**, 519 (2010).
[32] J. Lee, J. Koo, Y. M. Jhon, and J. H. Lee, Opt. Express **23**, 6359 (2015).